Feed Horn Coupled Bolometer Arrays for SPIRE—Design, Simulations, and Measurements

Goutam Chattopadhyay, *Senior Member, IEEE*, Jason Glenn, James J. Bock, Brooks K. Rownd, Martin Caldwell, and Matthew J. Griffin

Abstract—In this paper, we present the design, modeling, and measurements of feed horn coupled large bolometer arrays being developed for the Herschel Space Observatory's Spectral and Photometric Imaging REceiver (SPIRE) instrument. SPIRE has five arrays of feed horn coupled silicon–nitride micromesh "spider-web" bolometers in two instruments, a three-band photometer, and a two-band Fourier transform spectrometer, each covering the 430-GHz–1.5-THz band. The optical coupling efficiency, bandwidth, and crosstalk between adjacent pixels of the arrays were investigated with numerical electromagnetic-field simulators, and prototype arrays were measured extensively in a test facility. The measured results were found to be in good agreement with simulation predictions, and the simulation results were used as a benchmark for the design goals of the instrument.

Index Terms—Feed horn coupled arrays, Fourier transform spectrometer (FTS), HFSS simulations, integrating cavities, photometer, spider-web bolometers.

I. INTRODUCTION

ONE OF THE pressing questions of modern astrophysics today is how galaxies and stars are formed. It is widely believed that the answer to that lies in the close study of the submillimeter and far-infrared (FIR) spectrum of the sky. Our universe is most luminous in this frequency range after the cosmic microwave background radiation. Radiation at these wavelengths where interstellar dust is transparent enables observations of star formation deeply embedded in molecular clouds. The Herschel Space Observatory (formerly known as FIRST) [1], [2]—a European Space Agency (ESA) *cornerstone* mission scheduled for launch in 2007, covers approximately the 60–700-μm (5 THz–430 GHz) range. The Spectral and Photometric Imaging REceiver (SPIRE) [3], [4] is one of the three cryogenic focal plane instruments on board the Herschel Space Observatory. The main scientific objectives of the SPIRE instrument are deep extragalactic and galactic imaging surveys

G. Chattopadhyay and J. J. Bock are with the Jet Propulsion Laboratory, California Institute of Technology, Pasadena CA 91125 USA.

J. Glenn and B. K. Rownd are with the Center for Astrophysics and Space Astronomy, University of Colorado at Boulder, Boulder, CO 80303 USA.

M. Caldwell is with the Rutherford Appleton Laboratory, Chilton, Didcot, Oxon. OX11 0QX, U.K.

M. J. Griffin is with the Department of Physics and Astronomy, Cardiff University, Wales CF10 3XQ, U.K.

and spectroscopy of star-forming regions in our own and other nearby galaxies.

SPIRE is composed of two complementary instruments, i.e., a three-band imaging photometer and a two-band imaging Fourier transform spectrometer (FTS), each covering the 200–700-μm (1.5 THz–430 GHz) band. Both instruments use 0.3-K feed horn coupled silicon–nitride (Si_3N_4) micromesh "spider-web" bolometers [5], which have been very successful in ground-based and sub-orbital millimeter-wave instruments. The multifrequency photometer instrument on SPIRE has three simultaneously imaging bolometer arrays with 139, 88, and 43 bolometers, in bands centered at 250-, 363-, and 517-μm wavelengths, respectively. The spectral resolution ($\lambda/\Delta\lambda$) of the broad-band photometer is around 3. The FTS instrument has two simultaneously imaging arrays of 37 and 19 bolometers, covering 200–325 and 306–670-μm wavelengths, respectively. The FTS arrays will be operated in continuous scan mode with adjustable optical path length, giving spectral resolution in the range of 1000–20 at 250-μm wavelength. The photometer and FTS arrays are not designed to operate simultaneously.

The design and development of large arrays of feed horn coupled bolometers at submillimeter wavelengths has come a long way. This is primarily due to the tremendous improvement in electromagnetic simulation capabilities over the last couple of years and recent advances in micromesh bolometer fabrication techniques, allowing high yield absorber arrays with bolometer detectors on individual silicon wafers. All these advancements were used in designing the SPIRE detector arrays. The photometer and FTS arrays in SPIRE are packed hexagonally on planar wafers sandwiched between a planar backshort plate and precision feed horn block. The feed horns are terminated in circular waveguides followed by integrating cavities formed by the backshort plate, silicon substrate wafer, and feed horn block. The monolithic design of the micromesh absorber and backshort wafer allows efficient packing of these arrays in a simple fixture.

II. DESIGN AND SIMULATIONS

A schematic of the SPIRE detector array, showing the details of a single pixel, is shown in Fig. 1. Each pixel has a conical feed horn connected to a circular waveguide. The horns for the array are constructed as a single piece by electroforming—electroplating copper on carbide-turned aluminum mandrels. To minimize heat capacity and cross section to cosmic ray
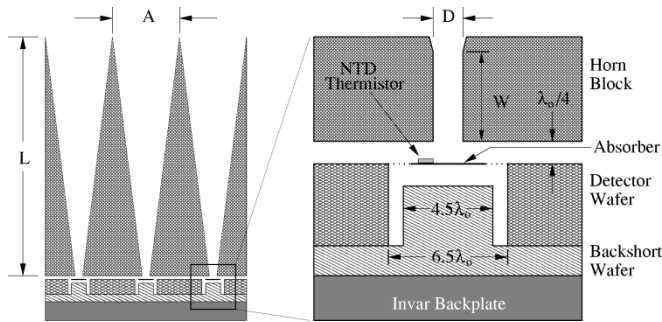
Fig. 1. Cross section of the SPIRE detector array showing the feed horns, circular waveguide section, and detector cavity. The drawing is not to scale. The dimensions labeled on this figure are listed in Table I for each of the photometer and FTS arrays. To give maximum overlap of the detectors in the focal plane, the horn center-to-center spacing was set $\approx 10\lambda_0$ for the photometers and $\approx 8\lambda_0$ for the spectrometers. The horn aperture is 100 μm less than the horn spacings to allow for 50-μm wall thickness. There is an vacuum gap of approximately $\lambda_0/4$ between the detector wafer and horn block. The length "L," shown on the left-hand side of the figure is to the apex of the horn.

TABLE I
FEED HORN AND CAVITY DIMENSIONS

Array	λ_0 (μm)	L (mm)	A (mm)	D (μm)	Waveguide Length (μm)
P/SW	250	23.68	2.40	171	500
P/MW	363	32.75	3.23	239	700
P/LW	517	46.36	4.90	342	1000
S/SW	275	23.68	2.15	190	550
S/LW	450	46.36	3.80	393	900

absorption, the bolometer absorbers have a "spider-web" architecture. The detector wafer has 1.8-μm–thick Si_3N_4 micromesh absorber patterned on a 350-μm-thick silicon substrate. Neutron-transmutation-doped (NTD) germanium (Ge) thermistors are indium (In) bump bonded to the absorbers. The detector wafer is mounted on a second metallized silicon wafer, which has been etched to form tuned backshorts. The detector wafer and backshort wafer combination is fixed to an invar backplate. Invar is used to minimize mechanical stress on silicon during thermal recycling and to keep the detectors aligned. The feed horn block is mounted on the invar backplate so that it is suspended over the detector wafer and maintains a safe vacuum gap between them. The lower half of the feed horn block, referred as the "frontshort," and the backshort along with the detector form the integrating cavity. The cavities are circularly symmetric about the axis of the circular waveguides connected to the feed horns. The integrating cavity has a diameter of $6.5\lambda_0$ with a $4.5\lambda_0$–diameter micromesh absorber sitting at approximately $\lambda_0/4$ distance from both the frontshort and backshort for optimum absorption. λ_0 is the free-space wavelength at the band center of the different photometer and the FTS arrays. It can be seen from Fig. 1 that there is a $\lambda_0/4$ vacuum gap in each pixel, which will allow cavity energy to leak from one pixel to the other, possibly degrading isolation between adjacent cavities. For convenience, the five SPIRE detector arrays have been designated "P/SW," "P/MW," and "P/LW" for the short, medium, and long wavelength photometers, and "S/SW" and "S/LW" for the short and long wavelength spectrometers, respectively. For each array, the dimensions indicated in Fig. 1 are listed in Table I.

A. Simulation Setup

The basic objective of our simulations was to design, optimize, and predict performance of the bolometric integrating cavities. We used Ansoft's *High Frequency Structure Simulator* (*HFSS*)[1] for simulating SPIRE's integrating cavities. *HFSS* solves electromagnetic-field parameters in arbitrary

[1]*High Frequency Structure Simulator (HFSS), Ver. 8*, Ansoft Corporation, Pittsburgh, PA.

three-dimensional structures using finite-element techniques. *HFSS* is ideal for our simulations because the calculated field quantities inside the cavities can be accessed, thereby allowing the optical coupling efficiency to be estimated. *HFSS* has been used before for integrating cavity coupling efficiency calculations by using a simple technique where the differences in the S-parameters, with and without the absorber inside the cavity, were used for predicting reflected and absorbed power in the cavity [6], [7]. *HFSS* has also been used to simulate complicated waveguide-based circuits such as solid-state frequency multipliers and ortho-mode transducers [8]–[10]. Due to the tremendous improvement in *HFSS* capabilities and phenomenal improvement of computer speeds over the last couple of years, it is now possible to carry out more sophisticated and detailed simulations and, consequently, to perform electromagnetic calculations to optimize and predict performance of large arrays of feed horn coupled integrating cavities.

Given that the cavities are larger than a wavelength, it was impossible to simulate an entire array in a single simulation using *HFSS*. Thus, we simulated an array of pixels by modeling a single pixel and using radiation boundary conditions on the outer walls of the pixel. Radiation boundaries absorb the energy incident on them. One could also use matching boundaries, also known as master–slave boundaries, to simulate periodic structures. Since the design was expected to have very low energy leakage between the pixels, both the radiation and matching boundary conditions would give similar results. We indeed checked this for our model and found the results obtained using both the radiation and the master–slave boundaries to be comparable. We also found that the simulation with radiation boundaries converged more quickly, making it the best choice for treating the boundary conditions for our simulations.

Fig. 2 shows the schematic of our single pixel model used for *HFSS* simulations. The top metal cover, which is a part of the horn block, is removed (shown upside down in this figure) to show the different components inside the cavity more clearly. Although, in reality, the micromesh absorbers are supported by thin silicon nitride legs, we suspended the absorbers in free space to simplify the model. Since the legs are thin (1.5 μm $\times$ 4 μm) and only one of them is metallized to carry detector bias, this simplification did not affect the simulations. The absorber itself was metallized to approximately match the free-space impedance to facilitate absorption. The metal backshort was realized using perfect E boundary condition on the protruded part of the backshort wafer, as shown in Fig. 2.

To determine the optical efficiency of the cavity, we needed to calculate the power absorbed by the absorber inside the inte-
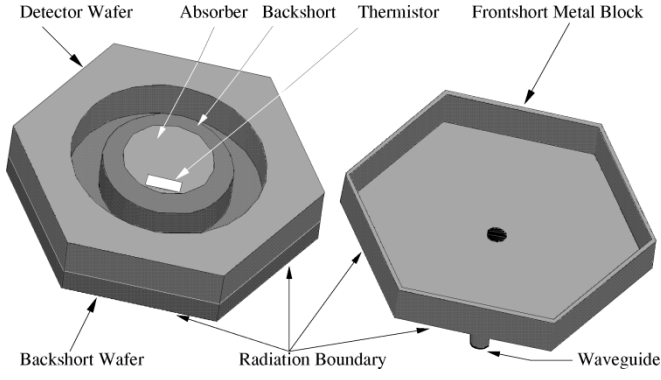
Fig. 2. Schematic of a single-pixel P/SW cavity used for *HFSS* simulations and the top metal cover removed with the frontshort shown upside down. The absorber is a 400-Ω/sq two-dimensional resistive sheet. Radiation boundaries are used at the silicon sidewalls and to simulate the vacuum gap between the silicon detector wafer and frontshort metal block.
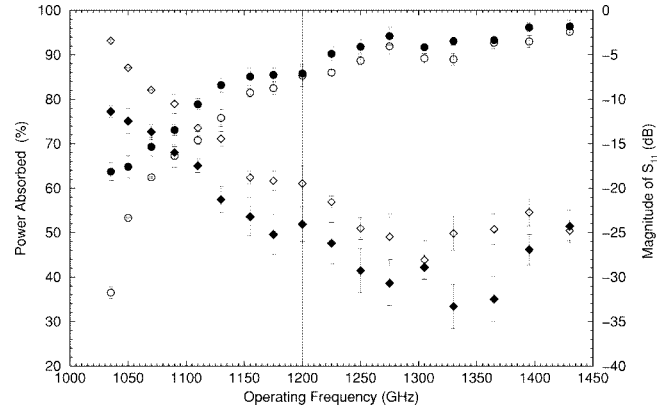

Fig. 3. Simulated performance of the P/SW cavity across the short-wavelength photometer band. The circles are for the absorbed power and the diamonds are for the return loss (the open circles and open diamonds are with a 171-μm-diameter waveguide and the filled circles and filled diamonds are with a 180-μm-diameter waveguide). The dotted vertical line shows the nominal band center frequency for which the different design parameters were optimized.

grating cavity. With *HFSS*, the electric and magnetic fields, current densities, and Poynting vectors can be integrated within the cavities. The power absorbed by a lossy medium can be calculated using a volume integral or a surface integral of the electric and magnetic fields [11]. Since we modeled our absorber as a two-dimensional sheet with surface resistance R_s, the absorbed power can be written as

$$P_{\text{absorbed}} = \frac{1}{2R_s} \int \int_S (\vec{E} \times \hat{n})^2 dS \qquad (1)$$

where $\hat{n}$ is the unit normal to the surface S. The surface resistance R_s was fixed at 400 Ω/sq for the simulations, which we previously found to be the optimum for these cavities [6], [12], [13].

We set up our simulations with a single-input port (the waveguide) and the dominant TE_{11}-mode excitation. For the multimode simulations, the waveguide port was excited with more than one mode, with the number of modes determined by the diameter of the over-moded waveguide. We carried out single-pixel simulations for the P/SW, S/LW, and S/SW cavities, and also a seven-pixel simulation for the P/SW cavity to predict leakage between adjacent cavities.

B. Error Estimation and Simulation Results

In *HFSS* port simulations, where S-parameters are calculated at different ports of a device, one can have a fair indication of the error in simulation through a parameter in the solution setup part of the solver. In the solution setup module, there is a term "Max Delta S," which is used as a stopping criteria in the adaptive meshing steps. When the magnitude and phase of all the S-parameters change by an amount less than the specified "Max Delta S" from one iteration to the next, the adaptive meshing stops, displaying the final "Delta S" value for the simulation. This parameter "Delta S" can be used as an indicator of simulation error for port simulations. We also used conservation of energy as a check: the integrated flux flowing out through the outer walls of the pixel, plus the power absorbed in the resistive layer should add up to the incident power at the input port (*HFSS* usually sets this power as 1 W). More often than not, there is some discrepancy between the calculated total power

and incident power, the extent of which depends on the coarseness of the mesh. This discrepancy in power can also be used in error estimation. For the simulation results presented here, the larger of these two error terms was taken as the calculation uncertainty.

Amongst the photometer arrays, the most extensive simulations were carried out on the short-wavelength photometer cavity (P/SW). This cavity has a 171-μm–diameter circular waveguide connected to the horn, and a backshort placed at a distance of 63 μm as the nominal design parameters. The simulated performance of the cavity across the intended operating frequency range of the instrument, with the backshort positioned at the nominal quarter-wave length distance, is shown in Fig. 3. It is clear from Fig. 3 that the power absorption and return-loss performance starts declining rapidly at around 1125 GHz, with only approximately 37% absorption (-5-dB return loss) at 1035 GHz. However, the performance at the upper end of the band was found to be much better. To improve optical coupling efficiency at the lower edge of the band, we decided to increase the diameter of the circular waveguide by approximately 5% to 180 μm. The cutoff frequency for the TM_{01} mode for this guide is 1276 GHz, compared to 1343 GHz for the 171-μm-diameter waveguide. The simulated performance of the P/SW cavity across the operating frequency band with a 180-μm-diameter waveguide and the backshort positioned at $\lambda_0/4$ showed substantial improvement in optical coupling efficiency across the band, specifically at the lower frequency end, as shown in Fig. 3. At 1035 GHz, power absorption increased to approximately 64% and return loss to -11 dB. Our simulations predicted only a marginal improvement in coupling efficiency with a further increase of the waveguide diameter. However, by increasing the waveguide diameter further, we pay the penalty of bringing the TM_{01} cutoff frequency even lower, right in the middle of the passband, and risk more mode conversions inside the cavity. As a result, we concluded that the P/SW design will certainly benefit from a 180-μm-diameter coupling waveguide. We ran simulations to optimize the backshort position for this design
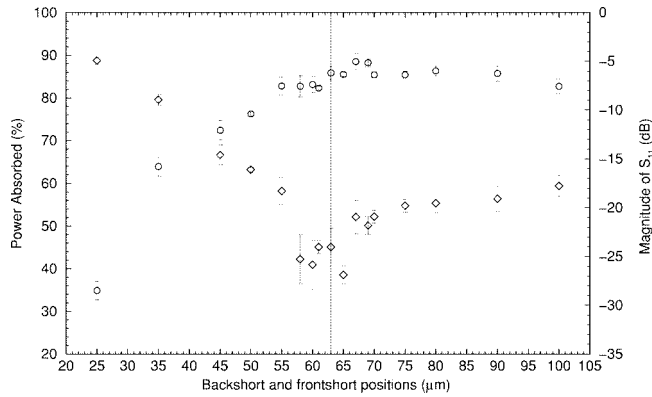
Fig. 4. Simulated performance of the short-wavelength photometer (P/SW) cavity with a 180-μm-diameter circular waveguide as a function of the backshort and frontshort positions. The circles are for the absorbed power and the diamonds are for the return loss. The dotted vertical line shows the nominal backshort and frontshort positions at $\lambda_0/4$.
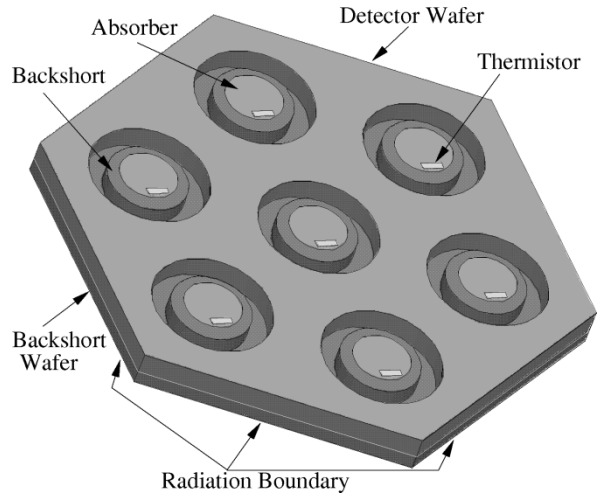

Fig. 5. Schematic of the seven-pixel simulation model for the P/SW cavity with the top metal cover (frontshort) removed. This model was used to determine the cross-coupling performance of the cavity.

and the result is shown in Fig. 4. It can be seen that the optimum backshort position is a few micrometers (≈ 5 μm) longer than the nominal $\lambda_0/4$ location. This slightly longer than a $\lambda_0/4$ backshort position can be attributed to the edge effects of the absorber where the fringe fields are created and they propagate inside the cavity with a different phase velocity.

In an attempt to investigate the possibility of using a highly over-moded waveguide for the P/SW and the S/SW cavities and study their coupling efficiency performance, we ran a few simulations with a 278-μm-diameter coupling waveguide. The cutoff frequencies for this guide are 632 GHz for the TE_{11} mode, 826 GHz for the TM_{01} mode, 1049 GHz for the TE_{21} mode, and 1316 GHz for the TM_{11} and TE_{01} modes. Since we wanted to evaluate the performance at the band center of the P/SW cavity, which is 1200 GHz, we ran simulations with the first three propagating modes, namely, TE_{11}, TM_{01}, and TE_{21}. First, we calculated coupling efficiencies with the waveguide input port excited with the three individual modes, excited independently one at a time, and then with all three modes excited simultaneously. At 1200 GHz, with the input port excited with the modes one at a time, 97% of the power was absorbed for the TE_{11} mode, 56% for the TM_{01} mode, and 78% for the TE_{21} mode. When the port was excited with all the three modes simultaneously, the total power absorbed was only approximately 72%. This low power absorption can be attributed to the interaction of the modes inside the cavity. Moreover, the higher order modes couple well to the background emission and not to the astrophysical sources since their beam patterns are not centrally peaked. Therefore, we abandoned the idea of using an over-moded waveguide and stuck with the 171-μm-diameter waveguide for the feed horn coupling, and not risk the additional coupling of the higher order modes.

It is important to pay close attention to the machining tolerances required for the frontshort metal block to avoid any possibility of crushing the detector wafer during assembly process. We ran simulations to investigate the allowable tolerance without significantly affecting the power absorption by varying the distance from the frontshort to the absorber, keeping the backshort position fixed at the optimum value, as shown in Fig. 4. We did not notice any substantial change

in power absorption due to the longer frontshort position from the absorber, up to approximately 40 μm more than the nominal $\lambda_0/4$ position. This indicates that the distance from the frontshort to the absorber is not quite as critical as the distance from the backshort to the absorber.

To investigate cross-coupling between adjacent pixels of the P/SW cavity, we simulated a seven-pixel model, as shown in Fig. 5. To calculate power leakage from one pixel to the other, we ran two different sets of simulations with two different input excitations. In the first case, we excited all six pixels surrounding the central pixel with the TE_{11} dominant mode at 1200 GHz. The pixel at the center of the model did not have any excitation at its input port and was terminated with a matched load. Power absorbed by the central pixel absorber under such excitations was calculated and was found to be less than 0.5%. In the second case, we only excited the pixel at the center of the array with the TE_{11} dominant mode at 1200 GHz, and terminated all other ports with matched loads. Similar to the first case, power absorbed by all other pixels in the immediate vicinity of the central pixel was found to be less than 0.5%, confirming very low cross-coupling between adjacent pixels.

For the spectrometer arrays, we simulated both the long- and the short-wavelength cavities. The S/LW and the S/SW cavities were simulated with 410- and 190-μm-diameter coupling waveguides, respectively. The simulated performance of the S/LW and S/SW cavities across the entire FTS band is shown in Fig. 6. For both spectrometers, the simulations were carried out with single-mode excitations, and the backshorts were optimized for the best coupling efficiency across the intended operating bands of the individual instruments. The results were found to be quite satisfactory, and we used them a benchmark for the design goals of the instrument.

III. FABRICATION, MEASUREMENTS, AND RESULTS

Fabrication of silicon–nitride micromesh bolometers has been described in detail by Turner *et al.* [14]. Here, we will elaborate on the fabrication aspects specific to the SPIRE instrument. For the detector wafer, a 1.8-μm-thick film of
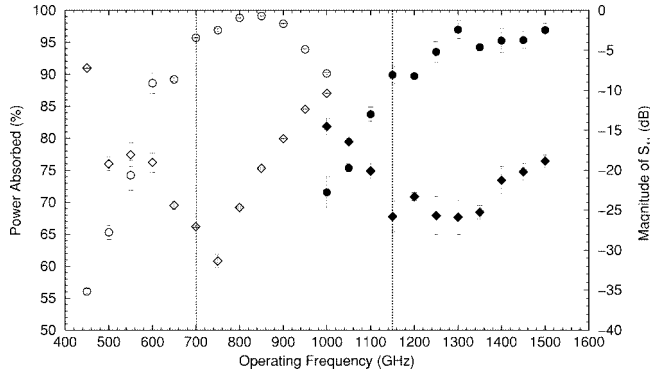
Fig. 6. Simulated performance of the S/LW and S/SW cavity across the FTS band. The diameter of the coupling waveguide was 410 μm for the S/LW band and 190 μm for the S/SW band. The open (S/LW) and closed (S/SW) circles are for the absorbed power, and the open (S/LW) and closed (S/SW) diamonds are for the return loss. The dotted vertical lines show the nominal band center frequencies for which the different design parameters for the S/LW and S/SW bands were optimized.
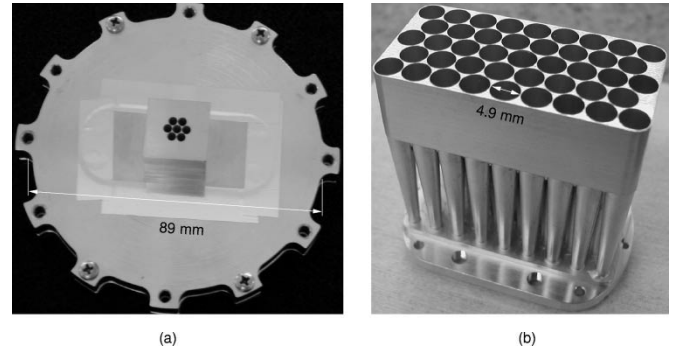

Fig. 7. Photographs of the fabricated arrays. (a) Prototype seven-pixel short-wavelength photometer (P/SW) testing detector array. (b) 43-pixel full-scale long-wavelength photometer (P/LW) horn array.

TABLE II
THEORETICAL AND MEASURED BEAM SIZES

Array	Band	Modes	Cal. HPBW	Mes. HPBW
P/SW	250 μm	TE_{11}	7.0°	6.8° $\pm$ 0.2°
S/LW	350 μm	$TE_{11}, TM_{01}, TE_{21}$	5.9°	9.8° $\pm$ 0.1°
S/LW	450 μm	TE_{11}, TM_{01}	7.3°	8.2° $\pm$ 0.3°

low-stress silicon nitride was deposited using low-pressure chemical vapor deposition (CVD) on a 100-mm-diameter 300-μm-thick silicon-on-insulator bonded silicon wafer. Using liftoff-photolithography technique, titanium–gold (Ti–Au) metal film was deposited to form the absorber layer, wiring leads, and contact layer. Using argon (Ar) reactive ion etch (RIE), the Ti–Au layer was removed selectively to expose the absorber, and CF_4, and, O_2 RIE was used to selectively remove Si_3N_4 from the absorber surface. Similarly, using backside RIE processing, Si_3N_4 was removed to define the silicon frame of the detector wafer. The thermistors were developed from a polished NTD Ge wafer doped with 4.54×10^{16}/cm^3, concentration of gallium (Ga) and 1.29×10^{16}/cm^3, compensation of arsenic (Ar) [15]. The thermistor chips are approximately 300-μm long, 100-μm wide, and 25-μm thick. There are two 100 μm $\times$ 50 μm contact pads separated by 200 μm on the edges of the thermistors. The NTD Ge thermistors are attached at the edge of the absorber by In bump bonds with approximately 1–2 N of force using a micrometer. For the backshort wafer development, a silicon wafer was first coated with 5 nm of Ti and 500 nm of Au using liftoff lithography. The precise backshort dimensions for different photometer and FTS bands were then etched out using deep-trench RIE.

A photograph of a prototype seven-pixel short-wavelength photometer (P/SW) detector array, which was used for testing and verification of SPIRE design and simulations, is shown in Fig. 7(a). Fig. 7(b) shows a full-scale 43-pixel P/LW feed horn block fabricated by Custom Microwave Inc., Longmont, CO. Only two arrays, the P/SW and the S/LW, were chosen for testing as prototypes—the P/SW array was tested with a 250-μm bandpass, while the S/LW array was tested with both 350- and 450-μm bandpasses. We decided to test the S/LW array at two different frequency bands to have a better insight on the performance by resolving the test data as a function of wavelength.

The prototype arrays were installed in a liquid-helium cryostat with a closed-cycle ^{3}He cryocooler to cool the focal plane to the 300-mK operational temperature. The prototype array optics included a filter stack consisting of a bandpass filter, a 0.9%-transmission neutral density filter (NDF), a stack of three or four nonparallel low-pass filters, and finally, a thin room-temperature high-density polyethylene (HDPE) Dewar window. The filters were installed on the radiation shields, with In gaskets to ensure light–tight interfaces and good thermal contact. The bolometers were configured in a balanced circuit and shared a common bias distributed through a load resistor array. The signal lines were buffered from external noise sources by low-noise source–follower junction field-effect transistor (JFET) amplifiers kept at 130 K. A shielded pre-amplifier box mounted on the outside of the Dewar completed the amplifier chain.

The beams for the arrays were measured using a temperature-controlled blackbody source mounted on a two-axis linear track [16]. Each of the measured beams was fitted with a Gaussian model to determine their full-width half-maxima (FWHM). The case of unpolarized fully incoherent light was used in the Gaussian mode. The beam sizes derived from the Gaussian fits are shown in Table II, along with the expected half-power beamwidth (HPBW) calculated from the band center frequency and feed horn aperture for the TE_{11} mode alone. The single-mode 250-μm P/SW beam size was found to be consistent with the expected TE_{11}-mode diffraction limit; however, the multimode 350- and 450-μm S/LW beams were found to be larger by 68% and 15%, respectively. It is clear that the S/LW beams included contributions from the TM_{01} and TE_{21} modes, which were not centrally peaked.

The spectral responses of the detector and feed horn arrays were measured for each bandpass in combination with the filter stack using a Bruker IFS-120HR FIR FTS.[2] The experiment was set up to observe fringes from the spectrometer at the side exit port, with an HDPE lens to couple the beam to the focal plane. A representative measured FTS transmission spectra for each test band along with the expected bandpass profile for each filter
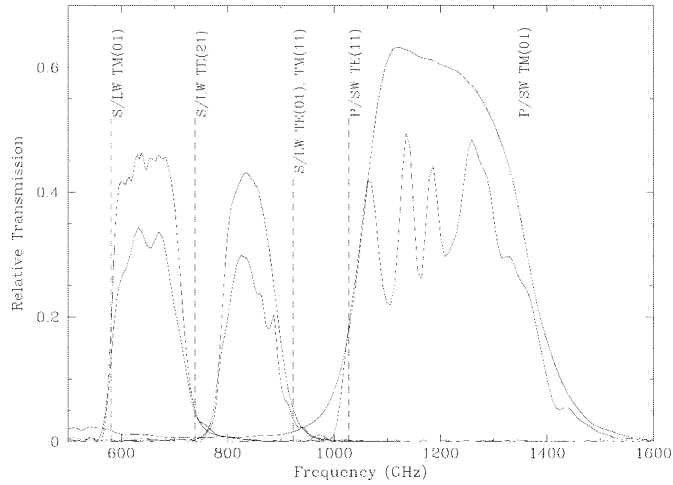
Fig. 8. Expected (upper) and measured (lower) bandpass transmission profiles are plotted together, along with the cutoff frequency markers for each mode of the waveguides in the P/SW and S/LW arrays. The measured and the expected relative transmissions are intentionally plotted here on a different scale for clarity. The structures in the measured spectra is due to the reflection from the Mylar beam splitter used in the measurement.

TABLE III
BANDPASS PROPERTIES

Array	Band	ν_0 (GHz) (measured)	$\Delta\nu$ (GHz) (measured)
P/SW	250 μm	1212	263
S/LW	350 μm	844	98
S/LW	450 μm	657	124

stack is shown in Fig. 8. The measured transmission spectra were found to be consistent with the expected centroid frequencies and widths of each bandpass, and their properties are tabulated in Table III.

The optical efficiencies of the detectors were derived from the *I–V* load curves measured under optical loading from blackbody sources at various temperatures, which completely filled the beams [16]. Measurements were made of blackbody sources external to the Dewar, as well as internal temperature-controlled "cold calibrator" blackbody source. The calculations presented here include a correction for 5% reflection off the surface of the liquid nitrogen, used as an external cold load, onto room temperature surfaces. The absorbed optical power is derived by measuring the offset in the electrical bias power dissipated in the detector along the lines of constant bolometer resistance. The hot and cold loads are measured in a cold–hot/hot–cold rotation so that any heating effect on the focal plane and the filters can be detected and removed to first order by averaging the data. Optical efficiencies derived in this method from the measured load curves are listed in Table IV. The listed uncertainties on the optical efficiencies are representative of the dispersion in the measurements for three different bolometers and horns, and do not include systematic errors. For the 250-μm P/SW band, which is mostly single moded, we measured an optical efficiency of 84%$\pm$3%, which is in good agreement with the 86% efficiency found at the center of the band in the simulations. The S/LW results are more complex due to the multimode nature of the

TABLE IV
OPTICAL EFFICIENCIES

Array	Band	ΔP (calculated) (pW)	ΔP (measured) (pW)	Optical Efficiency
P/SW	250 μm	10.7	8.6 $\pm$ 0.5	84 $\pm$ 3%
S/LW	350 μm	7.2	4.9 $\pm$ 0.2	69 $\pm$ 3%
S/LW	450 μm	3.8	2.1 $\pm$ 0.2	59 $\pm$ 3%

bands. For the 350-μm band, an optical efficiency of 69%$\pm$3%, was derived from measurements, assuming that the three propagating modes (two for the S/LW) are present with equal power in the bandpass. This specific cavity was not numerically simulated, but a comparison with the multimode simulation made for the P/SW model would provide some guidance in this regard. The multimode P/SW simulation yielded an optical efficiency of 72% when all three propagating modes were excited simultaneously, which agrees well with the 350-μm S/LW measurement. The 450-μm S/LW band has only two propagating modes, and it yielded a somewhat lower optical efficiency of 59%$\pm$3%. This indicates that the second dominant mode (TM_{01}) does not couple well to the detector by the horn and cavity, which is in agreement with the observation that the 450-μm beam size shows relatively less broadening from this mode than the S/SW. We also noticed from our P/SW simulations that the TM_{01} mode has the lowest absorption efficiency amongst the three modes.

Our simulations predicted that the leakage between adjacent bolometer cavities is less than 0.5%. Power leakage measurements were made with the 250-μm P/SW array. All but one of the feed horn apertures were blocked in the array, and the response to a chopped external blackbody signal on all the bolometers were measured with a lock-in amplifier. For the "dark" detector adjacent to the unobstructed feed horn, leakage was measured at 0.45% of the unobstructed detector's signal, with a signal-to-noise ratio of 3. This demonstrates that the leakage (crosstalk) is indeed low, which is consistent with our simulation results.

IV. CONCLUSION

In this paper, we have described a new modeling technique using the *HFSS* three-dimensional electromagnetic-field solver to numerically simulate large arrays of feed horn coupled integrating bolometric cavities. The simulations were detailed, and gave us access to field parameters inside the bolometer cavities to efficiently design, optimize, and predict performance of large format bolometer arrays, such as the SPIRE instrument. Measurements carried out on a seven-pixel prototype array allowed us to compare the simulation results with measured data, and they were found to be in close agreement. The beam sizes obtained from beam measurements and the spectral responses from FTS measurements were found to be consistent with the design theory. The optical coupling efficiency of the arrays, derived from the measured data, were found to be within a few percent of the simulated predictions, both for single-mode and multimode excitations. Low levels of crosstalk, as predicted by simulations, were corroborated by the measured low-leakage between adjacent cavities.

REFERENCES

[1] G. L. Pilbratt, "The FIRST mission," in *Proc. Eur. Space Agency Symp.*, 1997, ESA SP-401.
[2] ——, "The Herschel mission, scientific objectives, and this meeting," in *Proc. Eur. Space Agency Symp.*, G. L. Pilbratt, J. Cermicharo, A. M. Heras, T. Prusti, and R. Harris, Eds., Dec. 2000, ESA SP-460, pp. 13–20.
[3] M. J. Griffin, L. Vigroux, and B. Swinyard, "SPIRE: A bolometer instrument for FIRST," in *Proc. SPIE*, vol. 3357, Kona, HI, May 1998, pp. 404–413.
[4] M. J. Griffin, B. Swinyard, and L. Vigroux, "The SPIRE instrument for Herschel," in *Proc. Eur. Space Agency Symp.*, G. L. Pilbratt, J. Cermicharo, A. M. Heras, T. Prusti, and R. Harris, Eds., Dec. 2000, ESA SP-460, pp. 37–44.
[5] P. D. Mauskopf, J. J. Bock, H. D. Castillo, W. Holzapfel, and A. E. Lange, "Composite infrared bolometers with Si_3N_4 micromesh absorbers," *Appl. Opt.*, vol. 36, no. 4, pp. 765–771, Feb. 1997.
[6] J. Glenn, G. Chattopadhyay, S. F. Edgington, A. E. Lange, J. J. Bock, P. M. Mauskopf, and A. T. Lee, "Numerical optimization of integrating cavities for diffraction limited millimeter-wave bolometer arrays," *Appl. Opt.*, vol. 41, no. 1, pp. 136–142, Jan. 2002.
[7] J. Glenn, J. J. Bock, G. Chattopadhyay, S. F. Edgington, A. E. Lange, J. Zmuidzinas, P. D. Mauskopf, B. Rownd, L. Yuen, and P. A. R. Ade, "Bolocam: A millimeter-wave bolometric camera," in *Proc. SPIE*, vol. 3357, Kona, HI, May 1998, pp. 326–334.
[8] G. Chattopadhyay, E. Schlecht, J. Gill, S. Martin, A. Maestrini, D. Pukala, F. Maiwald, and I. Mehdi, "A broadband 800 GHz Schottky balanced doubler," *IEEE Microwave Wireless Comp. Lett.*, vol. 12, pp. 117–118, Apr. 2002.
[9] G. Chattopadhyay and J. E. Carlstrom, "Finline ortho-mode transducer for millimeter waves," *IEEE Microwave Guided Wave Lett.*, vol. 9, pp. 339–341, Sept. 1999.
[10] G. Chattopadhyay, B. Philhour, J. E. Carlstrom, S. Church, A. Lange, and J. Zmuidzinas, "A 96-GHz ortho-mode transducer for the polatron," *IEEE Microwave Guided Wave Lett.*, vol. 8, pp. 421–423, Dec. 1998.
[11] R. F. Harrington, *Time–Harmonic Electromagnetic Fields*. New York: McGraw-Hill, 1987.
[12] M. D. Audley, private communication, Mar. 2002.
[13] W. D. Duncan, W. S. Holland, M. D. Audley, M. Cliffe, T. Hodson, B. D. Kelly, X. Gao, D. Gostick, M. MacIntosh, H. McGreger, T. Peacocke, K. Irwin, G. Hilton, S. Dieker, J. Beier, C. Teintsema, A. J. Walton, W. Parkes, T. Stevenson, A. Gundlach, C. Dunnare, and P. A. R. Ade, "SCUBA-2: Developing the detectors," in *Proc. SPIE*, vol. 4855, Waikoloa, HI, Aug. 2002, pp. 19–29.
[14] A. D. Turner, J. J. Bock, J. W. Beeman, J. Glenn, P. C. Hargrave, V. V. Hristov, H. T. Nguyen, F. Rahaman, S. Sethuraman, and A. L. Woodcraft, "Silicon nitride micromesh bolometer array for submillimeter astrophysics," *Appl. Opt.*, vol. 40, no. 28, pp. 4921–4932, Oct. 2001.
[15] E. E. Haller, "Physics and design of advanced IR bolometers and photoconductors," *Infrared Phys.*, vol. 25, no. 1–2, pp. 257–266, 1985.
[16] B. Rowand, J. J. Bock, G. Chattopadhyay, J. Glenn, and M. Griffin, "Design and performance of feedhorn coupled bolometer arrays for SPIRE," in *Proc. SPIE*, vol. 4855, Waikoloa, HI, Aug. 2002, pp. 510–519.

Goutam Chattopadhyay (S'93–M'99–SM'01) received the B.E. degree in electronics and telecommunication engineering from the Bengal Engineering College, Calcutta University, Calcutta, India, in 1987, the M.S. degree in electrical engineering from the University of Virginia, Charlottesville, in 1994, and the Ph.D. degree in electrical engineering from the California Institute of Technology, Pasadena, in 1999. His doctoral dissertation concerned the development of low-noise dual-polarized and balanced receivers at submillimeter wavelengths.

From 1987 to 1992, he was a Design Engineer with the Tata Institute of Fundamental Research (TIFR), Pune, India, where he designed local-oscillator systems for the Giant Meterwave Radio Telescope (GMRT) Project. In January 1993, he joined the Electrical Engineering Department, University of Virginia. Since September 1994, he has been with the Jet Propulsion Laboratory (JPL), California Institute of Technology, where he is currently a Senior Member of the Technical Staff. His research interests include microwave, millimeter-wave, and submillimeter-wave heterodyne and direct detector receivers, frequency sources in the terahertz region, antennas, superconductor–insulator–superconductor (SIS) mixer technology, and direct detector bolometer instruments.

Dr. Chattopadhyay is a member of Eta Kappa Nu. He was the recipient of the 1987 Best Undergraduate Gold Medal presented by the University of Calcutta, the 1992 Jawaharlal Nehru Fellowship Award presented by the Government of India, the 1997 IEEE Microwave Theory and Techniques Society (IEEE MTT-S) Graduate Fellowship Award, and the 2001 Award of Excellence presented by the JPL.

Jason Glenn was born in Albuquerque, NM, on November 8, 1968. He received the B.S. degree in physics from the University of New Mexico, Albuquerque, in 1992, and the Ph.D. degree in astronomy from the University of Arizona, Tucson, in 1997.

From 1997 to 1999, he was a Post-Doctoral Scholar in physics with the Observational Cosmology Group, California Institute of Technology, Pasadena. Since 2000, he has been an Assistant Professor of astrophysics with the University of Colorado at Boulder, and a Fellow of the Center for Astrophysics and Space Astronomy. His research interests include cosmology, the interstellar medium, and submillimeter- and millimeter-wave instrumentation for astronomy.

Prof. Glenn is a member of the American Astronomical Society (AAS).

James J. Bock received the B.S. degree in physics and mathematics from Duke University, Durham, NC, in 1987, and the Ph.D. degree in physics from the University of California at Berkeley, in 1990.

He is currently a Principal Scientist with the Jet Propulsion Laboratory, California Institute of Technology, Pasadena. He also holds a visiting faculty position with the Department of Physics, California Institute of Technology. He is the Principal Investigator from the U.S. for the SPIRE submillimeter camera and spectrometer to fly on the European Space Agency's (ESA's) Herschel Space Observatory. His research interests include cosmology and the detectors and instruments for astrophysics in far-infrared and millimeter wavelengths.

Dr. Bock was the recipient of the 1987 Julia Dale Prize presented by the Mathematics Department, Duke University, the 2001 Award of Excellence presented by the Jet Propulsion Laboratory, California Institute of Technology, and the 2002 Presidential Early Career Award for Science and Engineering.

Brooks K. Rownd received the B.S. degree in physics and B.S. degree in astrophysics from the University of Minnesota at Minneapolis–St. Paul, in 1993, and the M.S. degree in astrophysics from the University of Massachusetts at Amherst, in 2002.

He is currently with the Center for Astrophysics and Space Astronomy, University of Colorado at Boulder. His recent research has involved the construction and performance evaluation of prototype large-format silicon–nitride micromesh bolometer arrays for ground- and space-based millimeter-wavelength astronomical imaging.
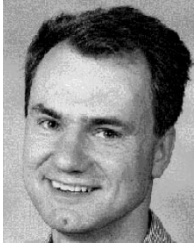
Martin Caldwell received the B.A. degree in physics from the University of Cambridge, Cambridge, U.K., in 1987, the M.Phil. degree in photodetector devices from the University of Sheffield, Sheffield, U.K., in 1989, and the Ph.D. degree from Imperial College, London, U.K., in 1991. His doctoral research was concerned the field of spatial light modulators based on liquid crystal.

He was subsequently an Optical Engineer with the GEC Marconi Research Center, Chelmsford, U.K., where he was involved with coherent laser radar systems for wind-speed measurement. This included development of eye-safe lasers at 2-μm wavelength and a bread-board wind-measurement demonstrator based on these lasers. In January 1994, he joined the Space Science Department, Rutherford Appleton Laboratory, Chilton, Didcot, Oxfordshire, U.K., where he is involved with a variety of optical instruments, mainly for space-borne applications in both earth remote sensing and astronomy. His projects include optical systems engineering for the Geostationary Earth Radiation Budget (GERB) earth-imaging broad-band radiometer, an earth radiation budget experiment in geostationary orbit and the development of optical design tools for diffractive propagation effects in far-IR instruments, initially for stray-light in limb-viewing radiometers in thermal-IR and later in the far-IR astronomy missions ISO-LWS and HERSCHEL-SPIRE. Since 2000 he has managed various studies on optical instruments for U.K. agencies and the ESA, e.g., radiation explorer in far-IR (REFIR), future visible and IR imager for Metop-3, and SMART-2 Optical Bench. He is currently the Systems Engineer for the IR Camera instrument on the VISTA ground-based telescope being built by the U.K. for the European Space Observatory (ESO).

Matthew J. Griffin received the Ph.D. degree in astrophysics with Queen Mary College London, London, U.K., in 1985.

He is currently a member of the Astronomy Instrumentation Group, Cardiff University, Wales, U.K. He is the Principal Investigator for the SPIRE submillimeter camera and spectrometer to fly on the ESA's Herschel Space Observatory. He is also a Co-Investigator of the High Frequency Instrument (HFI) for the Planck surveyor mission. His research interests have included instrumentation for far-IR and submillimeter astronomy and earth observation, planetary astronomy, and star formation.